Matter and Radiation at Extremes

RESEARCH ARTICLE

pubs.aip.org/aip/mre

Scilight Featured

Direct imaging of shock wave splitting in diamond at Mbar pressure

Cite as: Matter Radiat. Extremes 8, 066601 (2023); doi: 10.1063/5.0156681
Submitted: 2 May 2023 • Accepted: 1 August 2023 •
Published Online: 13 September 2023

Sergey Makarov,[1,a)] Sergey Dyachkov,[1] Tatiana Pikuz,[2] Kento Katagiri,[3,4] Hirotaka Nakamura,[3] Vasily Zhakhovsky,[1] Nail Inogamov,[5] Victor Khokhlov,[5] Artem Martynenko,[1] Bruno Albertazzi,[6] Gabriel Rigon,[6,7] Paul Mabey,[6,8] Nicholas J. Hartley,[9] Yuichi Inubushi,[10,11] Kohei Miyanishi,[11] Keiichi Sueda,[11] Tadashi Togashi,[10,11] Makina Yabashi,[10,11] Toshinori Yabuuchi,[10,11] Takuo Okuchi,[12] Ryosuke Kodama,[3,4] Sergey Pikuz,[1] Michel Koenig,[3,6] and Norimasa Ozaki[3,4]

AFFILIATIONS

[1]Joint Institute for High Temperatures of Russian Academy of Sciences, 13/2 Izhorskaya St., 125412 Moscow, Russia
[2]Institute for Open and Transdisciplinary Research Initiative, Osaka University, Suita, Osaka 565-0871, Japan
[3]Graduate School of Engineering, Osaka University, Suita, Osaka 565-0817, Japan
[4]Institute of Laser Engineering, Osaka University, Suita, Osaka 565-0871, Japan
[5]Landau Institute for Theoretical Physics of Russian Academy of Sciences, 1-A Akademika Semenova Ave., Chernogolovka, Moscow Region 142432, Russia
[6]LULI, CNRS, CEA, École Polytechnique, UPMC, Université Paris 06: Sorbonne Universités, Institut Polytechnique de Paris, F-91128 Palaiseau Cedex, France
[7]Graduate School of Science, Nagoya University, Chikusa Ku, Nagoya, Aichi 4648602, Japan
[8]Department of Physics, Experimental Biophysics and Space Sciences, Freie Universität Berlin, Arnimallee 14, 14195 Berlin, Germany
[9]SLAC National Accelerator Laboratory, 2575 Sand Hill Road, Menlo Park, California 94025, USA
[10]Japan Synchrotron Radiation Research Institute, Sayo, Hyogo 679-5198, Japan
[11]RIKEN SPring-8 Center, Sayo, Hyogo 679-5148, Japan
[12]Institute for Integrated Radiation and Nuclear Science, Kyoto University, Yoshida-honmachi, Sakyo-ku, Kyoto 606-8501, Japan

[a)]**Author to whom correspondence should be addressed:** seomakarov28@gmail.com

ABSTRACT

Understanding the behavior of matter at extreme pressures of the order of a megabar (Mbar) is essential to gain insight into various physical phenomena at macroscales—the formation of planets, young stars, and the cores of super-Earths, and at microscales—damage to ceramic materials and high-pressure plastic transformation and phase transitions in solids. Under dynamic compression of solids up to Mbar pressures, even a solid with high strength exhibits plastic properties, causing the induced shock wave to split in two: an elastic precursor and a plastic shock wave. This phenomenon is described by theoretical models based on indirect measurements of material response. The advent of x-ray free-electron lasers (XFELs) has made it possible to use their ultrashort pulses for direct observations of the propagation of shock waves in solid materials by the method of phase-contrast radiography. However, there is still a lack of comprehensive data for verification of theoretical models of different solids. Here, we present the results of an experiment in which the evolution of the coupled elastic–plastic wave structure in diamond was directly observed and studied with submicrometer spatial resolution, using the unique capabilities of the x-ray free-electron laser (XFEL). The direct measurements allowed, for the first time, the fitting and validation of the 2D failure model for diamond in the range of several Mbar. Our experimental approach opens new possibilities for the direct verification and construction of equations of state of matter in the ultra-high-stress range, which are relevant to solving a variety of problems in high-energy-density physics.

I. INTRODUCTION

Dynamic compression and shock loading of solid materials is a unique tool for the experimental study of their responses to ultrahigh strain rates and pressures.[1,2] A transition from an elastic to a plastic response is produced with a rise in loading stress. The pressure P_{HEL} at the Hugoniot elastic limit, at which such a transition occurs, is presented on the shock Hugoniot sketch shown on the left of Fig. 1. At pressures $P > P_{HEL}$, the material is subjected to plastic strain. At this stage, the shock wave may split into a fast elastic wave (precursor) and a slower plastic wave that follows it.[3–5] The study of elastic–plastic shock waves is extremely important, especially in planetology and asteroid impacts. Indeed, all material properties (yield strength, Poisson's ratio, and elastic and plastic wave structures and velocities) must be taken into account in numerical simulations of asteroid impact based on elastoplastic flow models. This is important to characterize the crater morphology (depth, diameter, etc.) generated by the different waves and to predict the consequences of an asteroid impact with Earth.[6] Separating and understanding the splitting mechanisms in shock-wave-induced plastic deformation in solids is of fundamental importance for developing accurate material models. One of the major problems in this field is the lack of accurate direct observational data to discriminate and validate models.

The most obvious, but at the same time extremely difficult, way to solve this problem is to directly visualize shock wave splitting in matter and resolve the elastic and plastic components. However, the splitting occurs at submicrometer scales, and the change in density, and hence contrast, with the waves is so low that it is impossible to do this using the traditional method of absorption radiography. To track shock wave evolution directly in visual observations, in particular elastic–plastic wave splitting in solids, first, it is necessary to use lighting parallel to the wave front (see Fig. 1) and, second, the material must be transparent to the radiation used. Diamond is a common object of study in research on material response to high pressures,[7–11] where the wave dynamics are analyzed in the direction normal to the shock front. This is done either by tracking the velocity of the diamond target boundary,[7–10] on which first the elastic wave and then the plastic wave sequentially emerge from the volume of a crystal, or by determining the reflectivity of the wave front.[12] However, in an extreme environment with pressures exceeding several megabars (Mbar), the physical characteristics of diamond are not well known, despite its common use in high-pressure anvil cells (DACs[13,14]). A shock wave with pressures of several Mbar travels at speeds of a few tens of km/s, and it is necessary to observe the stress state of the lattice and its temporal changes in real time. A broad and deep understanding of "diamond in the extreme environment" up to off-Hugoniot states is required for improving DAC performance and for understanding the internal structure of giant planets, the characteristics of warm dense matter (WDM), and the behavior of laser fusion fuel shells.

The methods that are conventionally used at high pressures, such as the velocity interferometer system for any reflector (VISAR)[4,15] and photon Doppler velocimetry (PDV),[4,16,17] can only probe a single surface and thus give only a limited idea of how shock waves behave inside a sample. Therefore, the state of a material as the shock wave propagates inside it can only be assessed by an indirect method. Absorption and phase-contrast x-ray methods based on a laser–plasma source[18,19] give a low image contrast, which is not enough to clearly resolve the regions inside the shock wave or the plastic shock wave. Therefore, it is difficult to establish accurate equations of state and verify theoretical models for the response of a substance under ultrahigh-pressure conditions.

The unique parameters of pulses generated by x-ray free electron lasers (XFELs) have opened a new branch of the study of matter under ultrahigh pressures. In particular, femtosecond XFEL pulses have begun to be used in x-ray diffraction (XRD) methods for measurement of shock-wave-driven twinning and lattice dynamics of solids[20] and the dynamic fracture of tantalum under extreme tensile stress.[21] There are two basic schemes for imaging with an XFEL probe using a focused and an unfocused beam. The first is a point projection scheme in which a magnified phase-contrast image is obtained by irradiation of the sample from the focusing point of the XFEL beam. This scheme is implemented at SLAC (the MEC station) and at EuXFEL (the MID station).[22–25] Such an approach allows simultaneous investigation of the sample with phase-contrast imaging and XRD techniques using a single XFEL pulse.[26] In this scheme, the spatial resolution is defined by the linear magnification and resolution of the detector. At the same time, the field of view depends on the distance between the focal point and the object. At present, a high spatial resolution is achieved by applying great magnification, and consequently the distance between the object and the detector must be increased to a few meters. The second approach allows a more compact experimental configuration and makes it easier to adjust the position of the object to provide optimal phase-contrast imaging conditions without changing of the field of view.[27,28] In this scheme, the spatial resolution is uniquely defined by the resolution of the detector. The first direct imaging of a shock wave passing into a solid using an XFEL pulse was obtained in 2015,[22] by combining a focused x-ray beam and a high-power laser. More recently, the first reports of visualization of shock waves in silicon using an XFEL have appeared.[29] In these works, a point projection scheme was used to probe the material.

Here, we use an XFEL source to make comparisons between direct observations in experiments and hydrodynamic simulations of wave splitting into an elastic shock precursor and a plastic shock wave in diamond. We used a phase-contrast imaging approach with unfocused XFEL probe beam and a lithium fluoride (LiF) fluorescent detector,[27] which has been successfully applied in recent studies of microscale phenomena in plasmas.[28]

The remainder of this article is organized as follows. In Sec. II, a description of the experimental scheme is given, together with an analysis of phase-contrast images of laser-induced shock waves produced in the target. A description of the simulation methods used in this work, as well as a comparison of numerical results with experimental data and a discussion, are presented in Sec. III. Our conclusions are presented in Sec. IV.

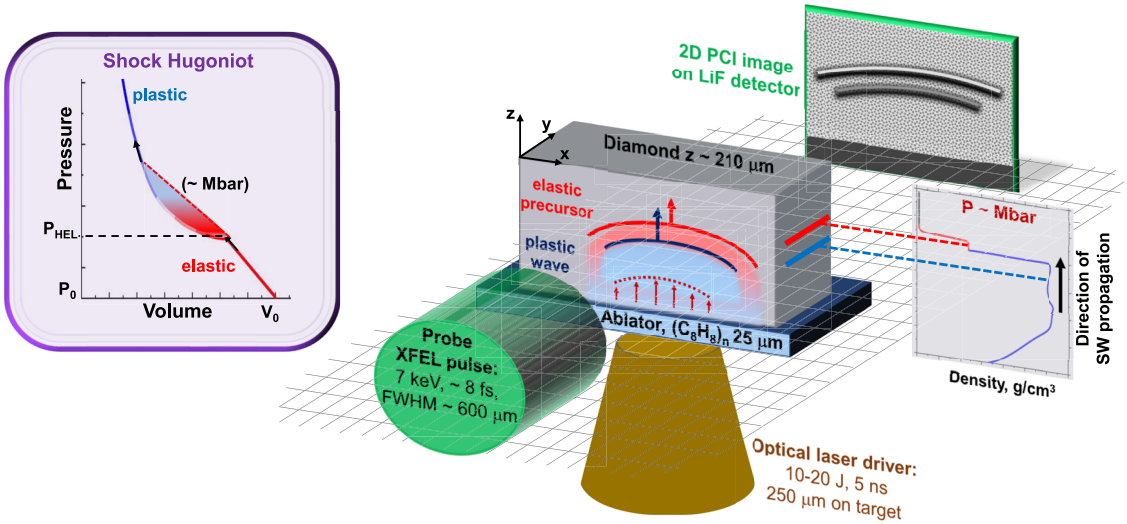

FIG. 1. Outline of pump–probe experiment for visualization of elastic–plastic shock wave (SW) evolution in diamond with submicrometer spatial resolution. A shock wave is driven by a focused drive laser (yellow) into a target consisting of an ablator (25 μm thick polystyrene) and a 210 μm thick monocrystalline diamond with crystallographic orientation ⟨100⟩ along the propagation direction of the laser. A 7 keV XFEL beam (green) probes the target with a delay of several nanoseconds with respect to the drive laser to observe the dynamics of the shock wave propagating in the diamond. An LiF detector is used to resolve the morphology of the low-contrast elastic–plastic shock waves with submicrometer spatial resolution.

II. EXPERIMENTAL RESULTS

A. Experimental setup

The experiment was performed at the SPring-8 Angstrom Compact Free Electron Laser (SACLA XFEL, Japan) at the experimental hutch EH5. A sketch of the experimental setup is shown in Fig. 1. The nanosecond optical driver pulse [laser wavelength 532 nm, pulse duration ~5 ns, pulse energy 10–20 J, full width at half maximum (FWHM) on sample 250 μm] was focused in the d_z direction on a multilayer target containing a thin layer of polystyrene ablator under the diamond sample and loaded it up to several Mbar pressure. The spatial and temporal profiles of the optical driver laser are shown in Fig. S1 (supplementary material).

The multilayer targets used for our experiment were composed of a polystyrene (1 g/cm^3) ablator and a monocrystalline type IIa diamond sample (3.51 g/cm^3) with dimensions $\Delta x \times \Delta y \times \Delta z = 2000 \times 2000 \times 25$ μm^3 and $\Delta x \times \Delta y \times \Delta z = 1500 \times 1500 \times 210$ μm^3, respectively. The diamond crystallographic orientation was ⟨100⟩ along the shock direction (which also corresponds to the direction of the driving optical laser) and ⟨010⟩ along the XFEL irradiation direction. The diamond samples were made by chemical vapor deposition and both 1500×1500 μm^2 surfaces were polished before the ablator was attached.

The evolution of the shock waves in the target was temporally resolved by irradiating the parallel XFEL beam (photon energy 7 keV, pulse energy 450 μJ, pulse duration 8 fs, divergence angle ~2 μrad, FWHM in the target plane 600 μm) in the d_y direction, with the delay being changed relative to the optical drive laser irradiation timing (Fig. 1). An ultrashort pulse duration of the XFEL beam provided a temporal resolution of the phase-contrast imaging platform in the femtosecond range (corresponding to a pulse duration of the probe beam $t \approx 8$ fs). An LiF fluorescent crystal detector was used to capture the phase-contrast pattern in the d_x–d_z plane with a submicrometer spatial resolution. For this, it was placed ~110 mm after the diamond sample, giving an optimal spatial resolution of 0.4 μm in our experimental geometry (see Fig. S1 and "Resolution and phase contrast approach" in the supplementary material). Note that when the shock is launched within the optical laser spot on the sample, it propagates through the ablator like a bubble in 3D. However, the XFEL probe projects this 3D elastic–plastic regime onto the LiF detector as a 2D image in the d_x–d_z plane.

B. Observation of shock wave propagation in diamond

The evolution of shock waves in the diamond sample was traced up to 12 ns after the beginning of the main laser pulse. In Fig. 2(a), we present a series of phase-contrast images recorded by the LiF detector at different delay times in the range from 3 to 12 ns. Note that the images shown here are not from a single laser shot, but rather from exposures with the same laser drive intensity ($I = 6 \times 10^{12}$ W/cm^2). The time at which the shock enters the diamond after the ablator has not been determined experimentally. To find this time, we simulated the interaction of the optical laser pulse with the ablator using the hydrodynamic code MULTI (see Sec. III A). We calculated that the shock wave generated in the ablator reached the diamond sample 2.05 ns after the start of the laser pulse with $I = 6 \times 10^{12}$ W/cm^2. For comparison with experimental data, Fig. 2(b) shows the results of the simulation of the shock wave evolution in diamond (the details and conditions of the simulation are presented in Sec. III B, together with a discussion of the results obtained).

The phase contrast enhancement and the submicrometer resolution of our experimental approach allowed us to clearly resolve

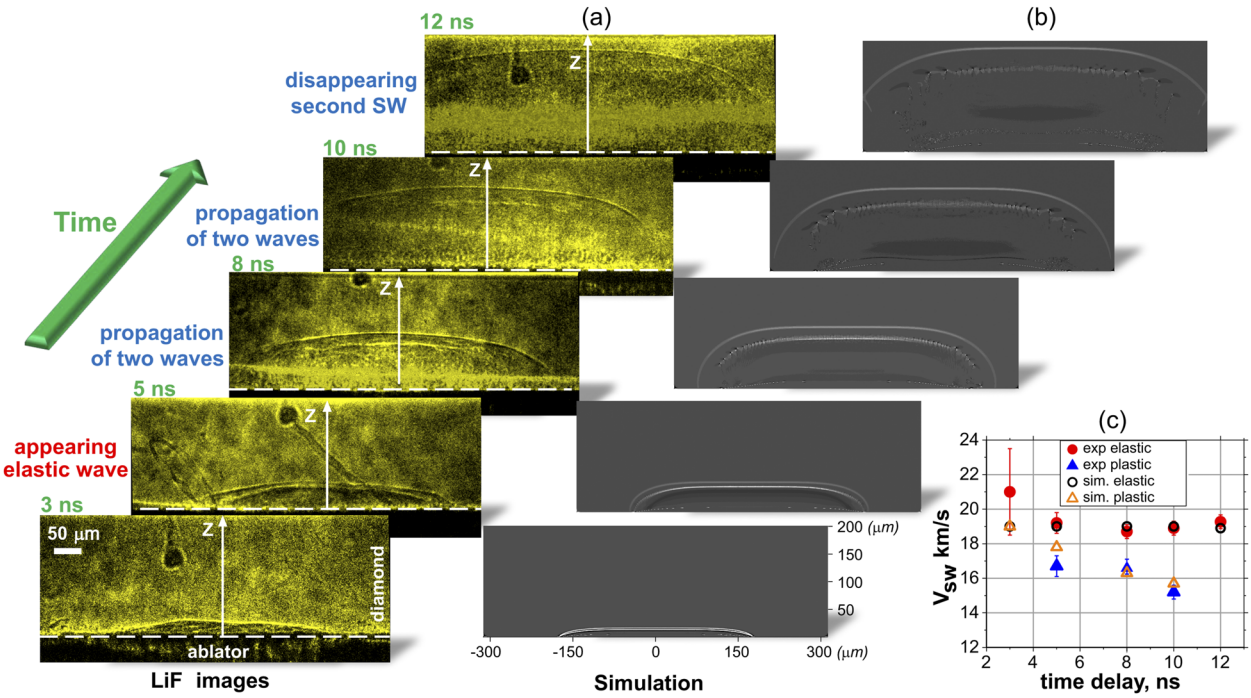

FIG. 2. Dynamics of shock wave evolution for times t = 3–12 ns after interaction of an optical laser of intensity $I = 6 \times 10^{12}$ W/cm^2 with the target. (a) Phase-contrast images of shock wave evolution in diamond taken with the LiF detector located at a distance of 110 mm from the target. (b) Results of smoothed particle hydrodynamics (SPH) simulation in 2D geometry (the strain rate map is shown). (c) Shock wave velocities at different times revealed from the experimental LiF image (red and blue dots) and the SPH simulation (black and orange dots).

the front of the generated shock wave, even though the difference in absorption between the shocked and unshocked regions of the diamond was less than 0.5% (more details are given under "Resolution and phase contrast approach" in the supplementary material). In the region behind the plastic wave, the remaining traces of the plastic deformation are visible.

At the initial stage of shock wave evolution (t = 3 ns), one can observe only a single shock wave in Fig. 2(a), which indicates that no noticeable wave splitting has occurred. At times in the range 3 ns < t < 5 ns, the shock wave splits into a clear two-wave structure in the diamond bulk, owing to the difference between the elastic and plastic wave speeds.[3] Such a regime emerges because P_{HEL} is exceeded: a plastic wave appears and begins to propagate in the elastically compressed material with the bulk sound speed according to the equation of state, while the elastic precursor outruns this wave under the effect of shear stresses. The observed shock wave is supported by the laser pulse for several nanoseconds, after which the release wave propagating from the ablator side reduces the plastic wave amplitude. As a result, the plastic wave front disappears completely in the range 10 ns < t < 12 ns, as shown in Fig. 2(a).

Using the data on the position of the shock wave fronts obtained from the radiographic LiF images in Fig. 2(a), the velocities of the shock waves observed in the experiment were reconstructed as they propagated inside the diamond. In Fig. 2(c), red and blue markers indicate the velocities obtained for elastic and plastic shock waves, respectively. It can be seen that the velocity of the precursor does not change as it passes through the diamond ($V_{elastic}$ = 19.0 ± 0.5 km/s), and it is in good agreement with previous results from VISAR[4,11] and x-ray imaging,[22] as well as the longitudinal elastic sound wave speed in the ⟨100⟩ direction of the diamond crystal.[30] At the same time, the plastic shock wave slows down (from $V_{plastic}$ = 21.0 ± 2.5 to 15.2 ± 0.5 km/s) and disappears between 10 and 12 ns [Fig. 2(a)]. This direct observation of plastic shock wave slowdown is an important result for model validation, especially with regard to VISAR, which only allows velocity evolution to be estimated by varying the target thickness or calculating the velocity averaged over the entire transit. For example, previous work[11] measured the velocity of the plastic shock wave to be $V_{plastic}$ = 13.64 ± 0.39 km/s for the same loading conditions of a ⟨100⟩-oriented diamond sample, but this was limited to probing the velocity at the rear surface, and could not see possible changes in speed as the shock wave propagated.

III. SIMULATION RESULTS AND DISCUSSION

To comprehensively investigate the state of a material under shock wave loading, it is necessary to know not only shock wave velocities, but also parameters such as pressure, density, ambient particle velocity, strain rate, and bulk and shear moduli. Although radiographic images only allow us to measure shock wave velocities and to obtain a linear density map, other parameters can be revealed from simulations. For this purpose, we performed a simulation of shock wave propagation inside the target.

Smoothed particle hydrodynamics (SPH) is widely used to model compressible materials with strength when they are subjected to extreme conditions. Under such conditions, propagation of shock waves may be accompanied by the development of instabilities, formation of cavities, material spallation, and fracture, which are difficult to model using conventional Eulerian or Lagrangian methods on a mesh. Most Eulerian codes and the aforementioned Lagrangian MULTI code do not include material strength, which is necessary to model the splitting of elastic and plastic shock waves. The meshless SPH approach allows such phenomena to be modeled naturally, without the need for complex algorithms to capture interfaces and free boundaries, and its Lagrangian formulation enables particle sizes to be adapted in accordance with the material strain.

The main reason for the application of SPH to the problem here is its ability to model of materials with strength when they are subjected to intense loads. Diamond has a uniquely high P_{HEL} of 0.5–0.8 Mbar and was subjected to loads up to several Mbar in our experiment. However, our SPH implementation lacks radiation transport support, and so MULTI modeling of the polystyrene–diamond interface was first performed to set up the appropriate boundary conditions.

A. Polystyrene response to pump laser

Modeling of laser ablation and shock wave generation in polystyrene was performed using the 1D radiation hydrodynamics code MULTI.[31] For the simulations, we used SESAME Table No. 7590 for polystyrene [gross chemical formula $(C_8H_8)_n$] and SESAME Table No. 7830 for diamond, with initial densities $\rho_1 = 1.1$ g/cm^3 and $\rho_2 = 3.52$ g/cm^3, respectively. The plastic thickness was set to 25 μm.

Figures 3(a) and 3(b) show the z–t diagrams as colormaps for the density and the pressure, respectively, from a particular MULTI simulation. They reveal the hydrodynamic processes occurring in the target at time and space intervals of 1–5 ns and 20–50 μm, respectively. The position 0 μm corresponds to the ablator–diamond interface, and the "front" part of the ablator at which the laser pulse arrives at time 0 ns (1% of the maximum laser intensity) is placed at $z = -25$ μm.

The laser pulse is absorbed in the polystyrene ablator, resulting in extreme heating and pressure growth. The ablated surface is evaporated and ionized, producing a plasma, and so the laser pulse continues to be absorbed in the area of the corona with a critical density (about two orders of magnitude lower than that in the solid ablator). A laser pulse of intensity $I = 6 \times 10^{12}$ W/cm^2 produces a pressure in the corona of about 2 Mbar, which keeps the bulk of the ablator from unloading until the end of the pulse. An initial shock wave propagates along the ablator to the interface with the diamond: the ablator layer is compressed by ~3 to 3.5 times (its thickness changes from 25 to ~6 to 8 μm) as the pressure increases to ~2 Mbar, which is close to the pressure at the laser ablation front as shown in Fig. 3 at 2–2.5 ns.

The shock wave reaches the interface between polystyrene and diamond at ~2.05 ns. The main shock wave begins to propagate through the diamond sample, while the reflected shock wave begins to propagate through the precompressed polystyrene, moving in the opposite direction, from the diamond boundary to the ablation front. This reflected shock wave passes the thin layer of the shocked ablator in 0.4 ns and reaches the ablation front. The shock wave is then reflected by this boundary and produces a spray of rarefaction waves, resulting in ablator expansion. The rarefaction wave reaches the surface of the diamond at ~2.7 ns and follows the main shock wave in the diamond bulk.

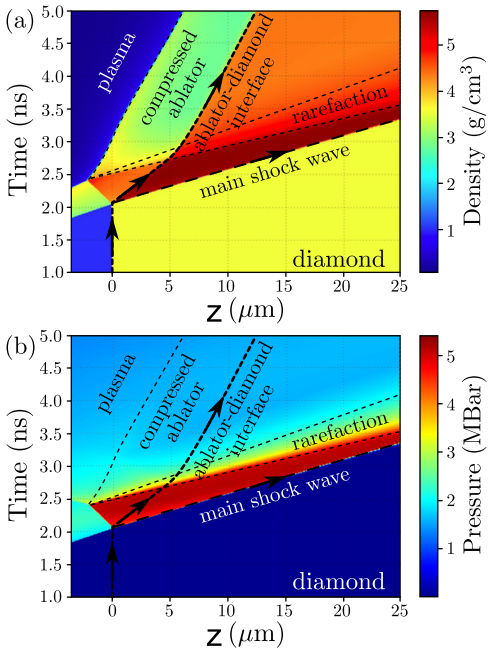

FIG. 3. (a) Density and (b) pressure maps obtained from 1D simulation using the radiation hydrodynamics code MULTI.

One can note a "triangle" of high density in the ablator, formed by the aforementioned shock wave that is reflected from the ablator–diamond interface [Fig. 3(a)]. The density in this triangle exceeds the initial density by 4.5–5 times, producing a pressure of ~4 Mbar, which is about twice the pressure in the plasma at the ablation front [Fig. 3(b)].

The release wave reaches the interface at ~2.7 ns, which is less than the pulse duration (5 ns). This leads to a pressure drop from ~4 Mbar to the pressure of the laser corona (~2 Mbar), which is sustained until the end of the laser pulse duration. The velocity of the ablator–diamond interface moves according to the applied pump: it accelerates to ~7 km/s by 2.7 ns. The end of the laser pulse is followed by a gradual decrease of pressure in the ablated plasma. As a result, the unburnt part of the ablator begins to be released, and it is pushed from the interface. The pressure on the diamond surface remains for a few tenths of a nanosecond until the "signal" indicating the end of the laser heating of the corona and zero pressure at the edge of the unburnt ablator reaches the diamond. The release leads to a gradual decrease in the interface velocity to almost zero.

The above mechanism is realized for laser pulse intensities starting from 10^{12} W/cm^2 and higher. For lower intensities of the order 10^{11} W/cm^2, the shock wave passing through the ablator reaches the ablator–diamond interface only after the end of the laser pulse.

The above simulations only consider a 1D case, but in reality there is spatial variation in the ablator–diamond interface velocity v_p. The laser intensity in our experiments is assumed to have a super-Gaussian distribution:

$$I(r) = I_0 \exp\left[\left(-\frac{e^2}{2R_0^2}\right)^3\right], \quad (1)$$

where $R_0 \approx 125$ μm is the radius of the laser spot, r is the distance from its center, and I_0 is the peak intensity.

To reproduce the response of a multidimensional ablator, we model the velocity $v_P(t)$ at various laser intensities $I \in (0, I_0]$ in the 1D MULTI code, and the values obtained are interpolated to give $v_P(t, I)$. The latter function is then transformed to $v_P(r, t) = v_P(t, I(r))$ and can be applied to model a multidimensional boundary condition at the ablator–diamond interface, if the transverse gradients of material velocity are notably smaller than the inwardly directed normal gradient along the z direction.

Figures 4(a)–4(c) show the results of MULTI simulations of velocity profiles and their interpolation. To construct $v_P(t, I)$, we calculated ten interface velocity profiles in MULTI for intensities $I \in [0.1, 1, 2, 3, 4, 5, 6, 7, 8, 9] \times 10^{12}$ W/cm^2, as shown in Fig. 4(a). The interpolation $v_P(t, I)$ thereby obtained is shown in Figs. 4(b) and 4(c). One can see that the higher-intensity pulses arrive at the ablator–diamond interface faster owing to a dramatic change in the ablator sound velocity at high compression. The arrival of the shock from the ablator leads to an extreme growth of velocity up to several km/s, which is followed by a small plateau and a gradual release.

Using the distribution (1), the function $v_P(t, I)$ is transformed to $v_P(x, t)$, where the x axis is directed along the spot diameter, and the results are presented in Fig. 4(d) for several peak intensities I_0. One can see that the most intense load is formed around the center of the spot, which is followed by the fast release. However, one can also notice a ring at the periphery that produces some load after the release in the center, owing to the later arrival of a peripheric shock wave. The latter is clearly seen for $I_0 = 3 \times 10^{12}$ W/cm^2 in Fig. 4(d). It is unclear whether this effect is an artifact of the interpolation, or whether it may appear in real simulations of 2D or 3D laser radiation absorption. Nevertheless, such small distortion at the periphery does not affect the propagation of a main shock wave in diamond, as we can see from the following SPH simulation results.

B. Failure model for diamond under shock loading

As has recently been shown,[4,32] the available models of metal plasticity are not suitable for describing the mechanical deformation of shock-compressed diamond single crystals at stresses beyond the Hugoniot elastic limit. McWilliams *et al.*[11] noted that diamond is a brittle material, the response of which is close to that of silicon

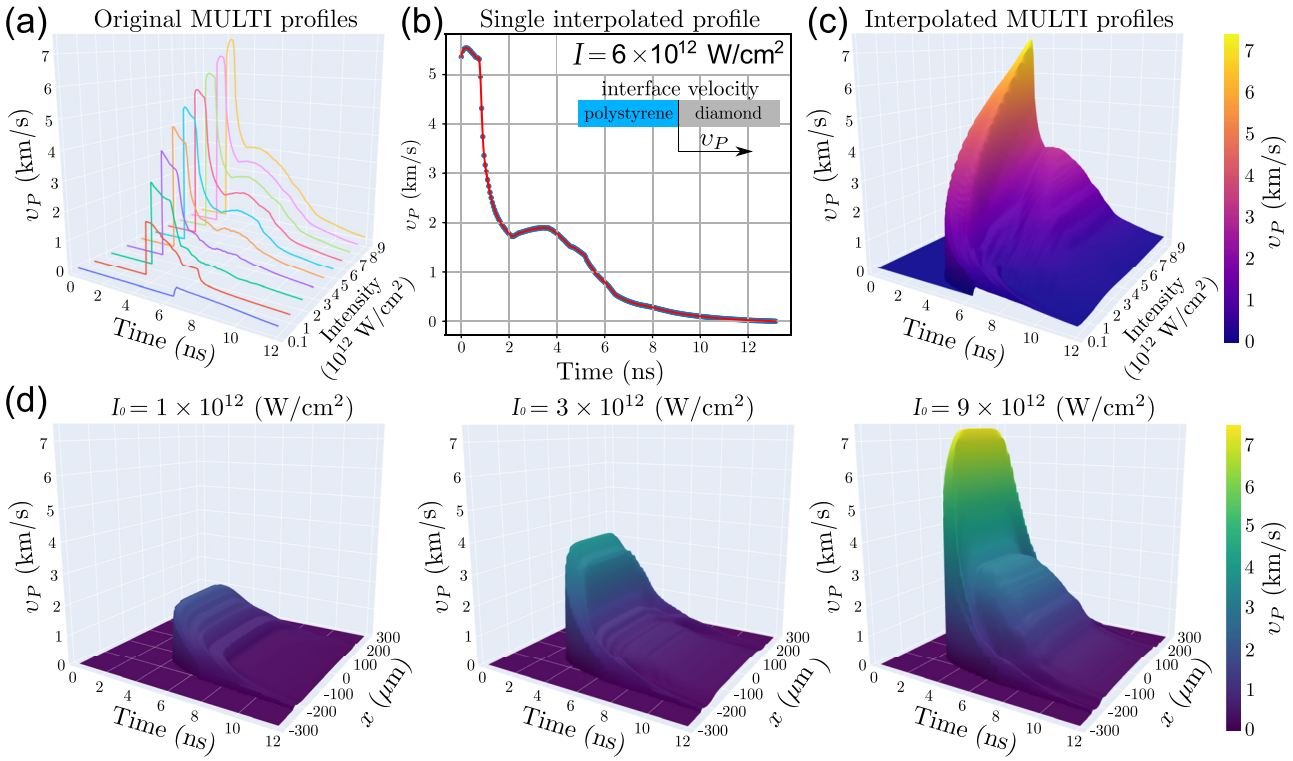

FIG. 4. (a) Velocity profiles v_P (t) of the ablator–diamond interface obtained in 1D MULTI simulations for various intensities. (b) and (c) Results of the velocity profile interpolation $v_P(t, I)$ required for further multidimensional SPH simulations with strength. (d) Velocity profiles $v_P(x, t)$, where the x axis is directed along the spot diameter, obtained using the spatial laser intensity profile for different peak intensities $I_0 = 1 \times 10^{12}$, 3×10^{12}, and 9×10^{12} W/cm^2.

carbide ceramics, whose strength degrades because of material failure at shock loads above the Hugoniot elastic limit. In our study, we used a failure model[33] developed for strong ceramic materials such as boron carbide and silicon carbide. This model assumes that the strength of the intact material loaded to the Hugoniot elastic limit begins to degrade with accumulation of plastic strain until the lower strength boundary (failed material strength) is reached. The shapes of the intact and failed material strength curves as functions of pressure and strain rate guide the kinetics of the failure process.

The model parameters were first calibrated using the VISAR data on uniaxial shock compression of diamond crystal in the ⟨100⟩ direction provided by McWilliams *et al.*[11] To obtain preliminary parameters of the failure model for diamond, we performed numerical simulations of the tests dh2, dh9, and dh18 (Fig. S4, supplementary material). It is worth noting that our failure model is isotropic, but, being calibrated for the ⟨100⟩ direction, it should be consistent with our XFEL observations. The impact in the experiments described in Ref. 11 was performed using an intense laser pulse applied to an aluminum buffer, and so the impactor velocity was estimated according to the velocity plateau achieved at maximum compression. The width and height of the elastic precursor and the kinetics of failure were adjusted by varying Poisson's ratio and the shape of the intact and failed material strength curves (more details can be found under "Diamond failure model" in the supplementary material).

In the framework of the failure model, 1D and 2D simulations were performed using an SPH code[34] to model the shock propagation in the diamond induced by the ablated layer of polystyrene (the details of the simulation can be found under "Continuum mechanics simulations" in the supplementary material). A comparison of

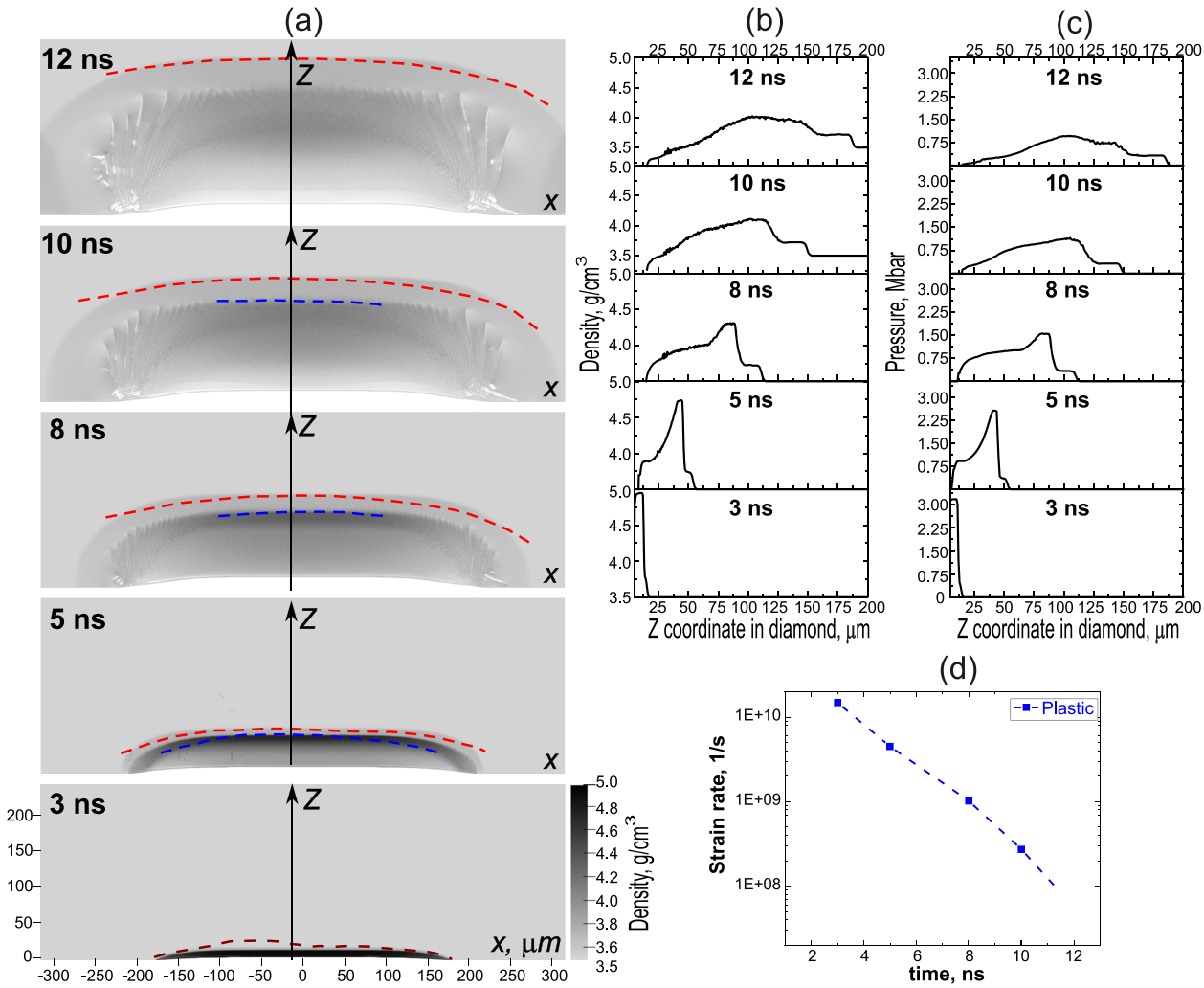

FIG. 5. Results of SPH simulations. (a) 2D maps of density. The experimental shock fronts have been digitized and superposed as dashed red (elastic) and blue (plastic) curves on the corresponding SPH results from the failure model. (b) Density and (c) pressure data retrieved along the *Z* axis in case (a). (d) Strain rate value for plastic shock wave revealed by the SPH simulation.

the experimental LiF images and the 2D continuum mechanics simulation[35] is shown in Fig. 2. A two-wave shock structure—an elastic precursor followed by an inelastic compression wave—is observed under loading of single-crystal diamond compressed to peak stresses up to ~3 Mbar. As can be seen from a comparison of Figs. 2(a) and 2(b), the calculated SPH patterns successfully reproduce both the appearance of an elastic precursor at times 3 ns < t < 5 ns and the disappearance of the plastic shock front at times 10 ns < t < 12 ns, in agreement with the experimental radiographic images. There is also good agreement between the velocities of the observed waves, as can be seen in Fig. 2(c). For convenience, the experimental shock fronts are indicated by dashed curves superposed on the corresponding SPH results in Fig. 5(a). The density and pressure distributions along the Z direction are shown in Figs. 5(b) and 5(c).

As we saw in the experiment, the simulated elastic and plastic waves have not separated at 3 ns. The observed difference in the propagated distance at that time may be due to nonuniform heating of the ablator, which results in wave front distortion. At 5 ns, separation of the elastic precursor is seen in both experiment and simulation, and the observed and predicted wave speeds become close. At 8 ns, the waves have separated further, and the positions of the simulated shock fronts agree well with those in the experiment. The rarefaction wave overtakes the plastic wave at about 10 ns, and so it almost disappears: the predicted position of the remaining part still agrees with the experiment. Finally, although the plastic wave has disappeared at 12 ns, the elastic wave continues to propagate further. One should note the presence of oblique lines in the calculated density distributions in Fig. 5(a). These lines are the directions of destruction of the diamond under its loading.

The correspondence obtained is in agreement with the experiments by McWilliams *et al.*[11] that were used to fit the failure model of diamond. The best agreement between the experimentally measured and simulated velocities is achieved by setting the yield strength to 0.7 Mbar and Poisson's ratio to 0.1 (for more details, see under "Diamond failure model" in the supplementary material). It should be also noted that by directly comparing the experiment with the simulation, it was found that the strain rate in the plastic wave dropped from 1.5×10^{10} to 5.6×10^{7} s^{-1} [Fig. 5(d)].

The SPH simulation presented here demonstrates the possibility of reproducing the complex phenomena of wave splitting in the bulk of a material sample. The series of experimental images can be used to adjust the strength model precisely by tracking the positions of the shock fronts.

C. Estimation of density gradient in shock waves

As part of our study of shock wave morphology, we estimated a density gradient (the width of the shock wave fronts) using a method based on analysis of monochromatic x-ray images with high spatial resolution in phase contrast. For this, we performed a simulation of the phase-contrast images observed in the experiment to compare them with experimental data. The modeling of these images was performed using an open-access software framework for coherent and partially coherent x-ray wavefront propagation simulations, WavePropaGator (WPG).[36] The mathematical description used in WPG for modeling the propagation of XFEL radiation through composite targets is presented in detail in Ref. 27. As the probe, we considered an XFEL beam with the same initial parameters as described earlier in this article.

Images corresponding to times t = 3 ns (one shock wave is observed) and t = 8 ns (two shock waves are clearly visible) were selected for analysis. To simulate the propagation of the SACLA beam through a shocked diamond sample, a number of independent parameters were introduced, including the density of the compressed material and the density gradients and density amplitudes of the shock waves (further details can be found under "Estimation

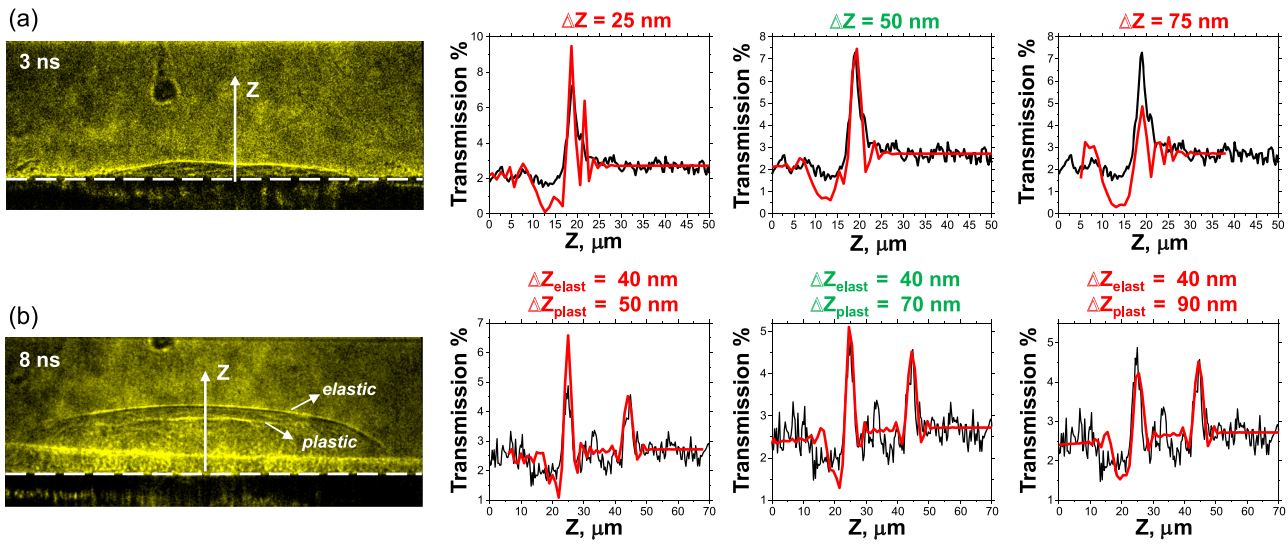

FIG. 6. Results of estimation of the front width ΔZ of shock waves observed in diamonds at times t = 3 ns (a) and t = 8 ns (b). The phase-contrast images on the left show the areas where the intensity distribution was recorded for the experimental profile. In the panels on the right, the experimental and simulated profiles along the Z direction are shown by the black and red lines, respectively.

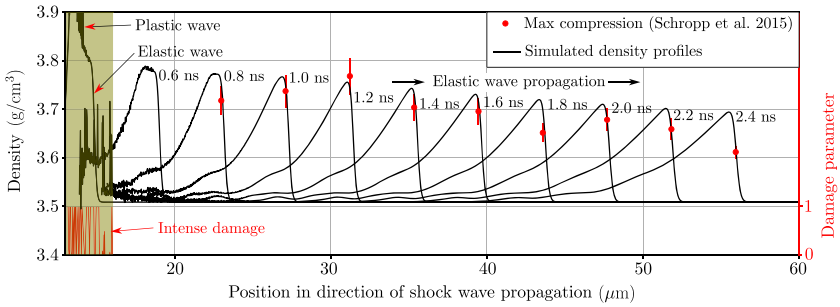

FIG. 7. Shock wave profiles in diamond under the laser intensity ~1.2 × 10^{13} W/cm^2 used in Ref. 22: the experimental data for maximal compression detected during shock propagation are placed at positions calculated with a fixed shock speed V = 20.6 km/s (within the range 19.9 ± 1.7 km/s[22]). The 1D SPH simulation performed using the diamond model calibrated with our experimental data also agrees with the data of Schropp *et al.*[22] SPH reveals the existence of a plastic wave at early times, which should completely decay by 0.6 ns, and so it could not be detected in the experiments by Schropp *et al.*[22]

of density gradient in shock waves" in the supplementary material). After setting up the incident beam and the transmission plane (target), we propagated the wavefront using a free-space propagator over a distance of 110 mm to the observation plane (LiF detector). By fixing parameters retrieved from SPH simulations [the density distribution in the diamond sample along the propagation direction of the shock wave, as shown in Fig. 5(b)] and by varying the density gradients of the shock waves at the fronts, we found the solutions describing the experimental phase-contrast image profiles for the time delays of 3 and 8 ns. We found that the width of the elastic–plastic structure at 3 ns was 50 nm, and the widths of the fronts at 8 ns were 40 and 70 nm for the elastic and plastic shock waves, respectively (Fig. 6). These estimates are an order of magnitude higher than the values expected from theoretical considerations (of the order of the interatomic lattice spacing), which could be due to two reasons:

- We do not observe a flat shock wave front, but a curved one, which blurs the experimental profile of the phase-contrast image.
- The detector resolution obviously increases the experimentally measured profile, which is then compared with the model.

D. Discussion

Several advantages of our experimental–theoretical approach compared with existing approaches should be mentioned, to avoid researchers from misunderstanding their data:

- VISAR does not allow the measured velocities to be directly associated with specific waves. This problem is even more severe when the material under study is opaque to visible light. Information is then transported to the rear surface of the sample, where it is mixed, and analysis is much more difficult (see, e.g., Ref. 11). In addition, it should be noted that the loss of stability of the surface of the test sample during melting can lead to a strong decrease in its reflectivity due to a strong shock wave effect, which limits the range of application of interferometric methods in the study of shock wave processes.
- The decrease in the plastic wave velocity observed in our work is a crucial parameter to benchmark the experimental data against numerical simulations and help constrain material properties (yield strength and Poisson's ratio).

The experimental scheme presented in this study allows us to overcome these difficulties, since the two-wave structure is clear in our data. At first sight, the presence of a paired wave structure in diamond pumped with a ~6 TW/cm^2 laser is in contradiction with the study by Schropp *et al.*,[22] in which an experiment was performed with diamond at approximately twice the laser drive intensity. The propagation of a shock wave was recorded in phase-contrast images, but the splitting regime was not observed. To resolve this contradiction, we performed further SPH modeling using the diamond model calibrated with our experimental data, assuming the experimental conditions of Shropp *et al.*[22]

Figure 7 shows the results of the 1D calculations, which show the presence of a plastic shock wave splitting from the elastic shock front in the early stage of wave evolution. The wave splitting is visible after 0.4 ns, but the plastic wave decays by 0.6 ns, which makes it difficult to observe this phenomenon in the study by Schropp *et al.*[22] Our simulation shows that the intense damage caused by the plastic wave after the intense loading introduces density fluctuations into the material. The plastic wave leaves a region of damaged material, which corresponds to the trace of plastic deformations in the form of a dark zone with fixed width of 13–15 μm observed in the phase-contrast images.[22] The strain produced by the elastic wave is reversible, and so the diamond unloads to near-normal density. It should be noted that this elastic wave gradually decays, but in the study by Schropp *et al.*[22] it was found to be faster owing to unloading from the free boundaries of the sample, which was not accounted for in our 1D simulation. Nevertheless, the wave speed observed in our simulation agrees well with the shock velocity V = (19.9 ± 1.7) km/s measured by Schropp *et al.*[22]

IV. CONCLUSION

In this article, we have taken a significant step in the further implementation of the phase-contrast approach by using an unfocused XFEL probe beam and, for the first time, directly

resolving the splitting of a shock wave into an elastic precursor and a plastic shock wave in diamond. We have succeeded in tracing the evolution of the structure from the moment of appearance of the elastic precursor up to the stage of disappearance of the plastic shock wave at submicrometer resolution, as well as the remaining traces of plastic deformation. A single direct measurement allows one to validate a strength model for diamond in the range of several Mbar. The excellent agreement achieved between experimental data and continuum mechanics modeling shown in our work not only paves the way for direct measurement of the dynamic yield strength of materials as a function of strain rate, but also highlights the usefulness of XFEL facilities for the study of high-speed crack dynamics and unusual stress-induced solid-state phase transitions. The combined experimental–theoretical approach presented here opens new horizons in the development of models and the validation of pressure-driven shock wave simulations. This goes well beyond equation-of-state measurements using VISAR, by allowing observations of the continuous evolution of the two-wave structure and of evolution throughout the depth of the target, thus enabling the extraction of much more information about the processes involved, as well as direct comparison with simulated data.

SUPPLEMENTARY MATERIAL

The supplementary material contains an extended description of the methods used for the study presented in the article.

ACKNOWLEDGMENTS

We thank the technical staff of SACLA for their support during the experiment. The experiment was performed at BL3 of SACLA with the approval of the Japan Synchrotron Radiation Research Institute (Proposal Nos. 2021A8004 and 2021B8002). The high-power drive laser installed in SACLA EH5 was developed with the cooperation of Hamamatsu Photonics. The installation of diffractive optical elements to improve the smoothness of the drive laser-pattern was supported by the SACLA Basic Development Program.

The work was carried out with the financial support of the Russian Federation represented by the Ministry of Science and Higher Education of the Russian Federation (Grant No. 075-15-2021-1352). This work was supported by KAKENHI (Grant Nos. 17K05729 and 21K03499) from the Japan Society for the Promotion of Science (JSPS).

AUTHOR DECLARATIONS

Conflict of Interest

The authors have no conflicts to disclose.

Author Contributions

N.O. and M.K. conceived the project. T.P., H.N., G.R., B.A., P.M., M.K., N.J.H., K.K., Y.I., K.M., K.S., T.T., M.Y., T.Y., T.O., and N.O. performed the experiment. MULTI simulations were performed by A.M. SPH simulations were performed by S.D. WavePropaGator simulations were performed by S.M. S.M. analyzed the experimental data and interpreted the experimental results with S.D., T.P., S.P., V.Z., N.I., R.K., and V.K. The paper was written by S.M. and S.D. All coauthors commented on the manuscript.

Sergey Makarov: Investigation (equal); Validation (equal); Visualization (equal); Writing – original draft (equal). **Sergey Dyachkov**: Investigation (equal); Software (equal); Validation (equal); Writing – review & editing (equal). **Tatiana Pikuz**: Investigation (equal); Methodology (equal); Writing – review & editing (equal). **Kento Katagiri**: Methodology (equal); Writing – review & editing (equal). **Hirotaka Nakamura**: Methodology (equal). **Vasily Zhakhovsky**: Investigation (equal); Validation (supporting); Writing – review & editing (supporting). **Nail Inogamov**: Investigation (equal); Writing – review & editing (supporting). **Victor Khokhlov**: Investigation (equal); Writing – review & editing (supporting). **Artem Martynenko**: Investigation (supporting); Validation (equal); Writing – review & editing (supporting). **Bruno Albertazzi**: Methodology (equal); Writing – review & editing (supporting). **Gabriel Rigon**: Methodology (equal). **Paul Mabey**: Methodology (equal); Writing – review & editing (supporting). **Nicholas J. Hartley**: Methodology (equal); Writing – review & editing (equal). **Yuichi Inubushi**: Methodology (equal). **Kohei Miyanishi**: Methodology (equal). **Keiichi Sueda**: Methodology (equal). **Tadashi Togashi**: Methodology (equal). **Makina Yabashi**: Methodology (equal). **Toshinori Yabuuchi**: Methodology (equal). **Takuo Okuchi**: Methodology (equal). **Ryosuke Kodama**: Writing – review & editing (supporting). **Sergey Pikuz**: Investigation (equal); Writing – review & editing (supporting). **Michel Koenig**: Conceptualization (equal); Writing – review & editing (supporting). **Norimasa Ozaki**: Conceptualization (equal); Writing – review & editing (supporting).

DATA AVAILABILITY

The data that support the findings of this study are available within the article and its supplementary material. The data that support the findings of this study are available from the corresponding author upon reasonable request. The SPH, MULTI, and WavePropaGator codes used for this study are available on reasonable request from S.D. (serj.dyachkov@gmail.com), A.M. (martynenko.art@gmail.com), and S.M. (seomakarov28@gmail.com), respectively.

REFERENCES

[1]T. S. Duffy and R. F. Smith, "Ultra-high pressure dynamic compression of geological materials," Front. Earth Sci. **7**, 23 (2019).
[2]S. Brygoo, E. Henry, P. Loubeyre, J. Eggert, M. Koenig, B. Loupias, A. Benuzzi-Mounaix, and M. Rabec Le Gloahec, "Laser-shock compression of diamond and evidence of a negative-slope melting curve," Nat. Mater. **6**, 274–277 (2007).
[3]G. I. Kanel, V. E. Fortov, and S. V. Razorenov, *Shock-Wave Phenomena and the Properties of Condensed Matter* (Springer, New York, 2004).
[4]J. M. Winey, M. D. Knudson, and Y. M. Gupta, "Shock compression response of diamond single crystals at multimegabar stresses," Phys. Rev. B **101**, 184105 (2020).
[5]S. J. Turneaure, P. Renganathan, J. M. Winey, and Y. M. Gupta, "Twinning and dislocation evolution during shock compression and release of single crystals: Real-time x-ray diffraction," Phys. Rev. Lett. **120**, 265503 (2018).

[6]G. S. Collins, H. J. Melosh, and R. A. Marcus, "Earth impact effects program: A Web-based computer program for calculating the regional environmental consequences of a meteoroid impact on Earth," Meteorit. Planet. Sci. **40**, 817–840 (2005).
[7]D. G. Hicks, T. R. Boehly, P. M. Celliers, D. K. Bradley, J. H. Eggert, R. S. McWilliams, R. Jeanloz, and G. W. Collins, "High-precision measurements of the diamond Hugoniot in and above the melt region," Phys. Rev. B **78**, 174102 (2008).
[8]M. D. Knudson, M. P. Desjarlais, and D. H. Dolan, "Shock-wave exploration of the high-pressure phases of carbon," Science **322**, 1822–1825 (2008).
[9]J. H. Eggert, D. G. Hicks, P. M. Celliers, D. K. Bradley, R. S. McWilliams, R. Jeanloz, J. E. Miller, T. R. Boehly, and G. W. Collins, "Melting temperature of diamond at ultrahigh pressure," Nat. Phys. **6**, 40–43 (2010).
[10]R. F. Smith, J. H. Eggert, R. Jeanloz, T. S. Duffy, D. G. Braun, J. R. Patterson, R. E. Rudd, J. Biener, A. E. Lazicki, A. V. Hamza, J. Wang, T. Braun, L. X. Benedict, P. M. Celliers, and G. W. Collins, "Ramp compression of diamond to five terapascals," Nature **511**, 330–333 (2014).
[11]R. S. McWilliams, J. H. Eggert, D. G. Hicks, D. K. Bradley, P. M. Celliers, D. K. Spaulding, T. R. Boehly, G. W. Collins, and R. Jeanloz, "Strength effects in diamond under shock compression from 0.1 to 1 TPa," Phys. Rev. B **81**, 014111 (2010).
[12]K. Jakubowska, D. Mancelli, R. Benocci, J. Trela, I. Errea, A. S. Martynenko, P. Neumayer, O. Rosmej, B. Borm, A. Molineri, C. Verona, D. Cannatà, A. Aliverdiev, H. E. Roman, and D. Batani, "Reflecting laser-driven shocks in diamond in the megabar pressure range," High Power Laser Sci. Eng. **9**, e3 (2021).
[13]H. K. Mao, "High-pressure physics: Sustained static generation of 1.36 to 1.72 megabars," Science **200**, 1145–1147 (1978).
[14]B. Li, C. Ji, W. Yang, J. Wang, K. Yang, R. Xu, W. Liu, Z. Cai, J. Chen, and H. k. Mao, "Diamond anvil cell behavior up to 4 Mbar," Proc. Natl. Acad. Sci. U. S. A. **115**, 1713–1717 (2018).
[15]L. M. Barker, "The development of the VISAR, and its use in shock compression science," AIP Conf. Proc. **505**, 11–18 (2000).
[16]O. T. Strand, D. R. Goosman, C. Martinez, T. L. Whitworth, and W. W. Kuhlow, "Compact system for high-speed velocimetry using heterodyne techniques," Rev. Sci. Instrum. **77**, 083108 (2006).
[17]T. Ao and D. H. Dolan, "Effect of window reflections on photonic Doppler velocimetry measurements," Rev. Sci. Instrum. **82**, 023907 (2011).
[18]F. Barbato, S. Atzeni, D. Batani, D. Bleiner, G. Boutoux, C. Brabetz, P. Bradford, D. Mancelli, P. Neumayer, A. Schiavi, J. Trela, L. Volpe, G. Zeraouli, N. Woolsey, and L. Antonelli, "Quantitative phase contrast imaging of a shock-wave with a laser-plasma based X-ray source," Sci. Rep. **9**, 18805 (2019).
[19]L. Antonelli, S. Atzeni, D. Batani, S. D. Baton, E. Brambrink, P. Forestier-Colleoni, M. Koenig, E. L. Bel, Y. Maheut, T. Nguyen-Bui, M. Richetta, C. Rousseaux, X. Ribeyre, A. Schiavi, and J. Trela, "X-ray absorption radiography for high pressure shock wave studies," J. Instrum. **13**, C01013 (2018).
[20]C. E. Wehrenberg, D. McGonegle, C. Bolme, A. Higginbotham, A. Lazicki, H. J. Lee, B. Nagler, H. S. Park, B. A. Remington, R. E. Rudd, M. Sliwa, M. Suggit, D. Swift, F. Tavella, L. Zepeda-Ruiz, and J. S. Wark, "*In situ* X-ray diffraction measurement of shock-wave-driven twinning and lattice dynamics," Nature **550**, 496–499 (2017).
[21]B. Albertazzi, N. Ozaki, V. Zhakhovsky, A. Faenov, H. Habara, M. Harmand, N. Hartley, D. Ilnitsky, N. Inogamov, Y. Inubushi, T. Ishikawa, T. Katayama, T. Koyama, M. Koenig, A. Krygier, T. Matsuoka, S. Matsuyama, E. McBride, K. P. Migdal, G. Morard, H. Ohashi, T. Okuchi, T. Pikuz, N. Purevjav, O. Sakata, Y. Sano, T. Sato, T. Sekine, Y. Seto, K. Takahashi, K. Tanaka, Y. Tange, T. Togashi, K. Tono, Y. Umeda, T. Vinci, M. Yabashi, T. Yabuuchi, K. Yamauchi, H. Yumoto, and R. Kodama, "Dynamic fracture of tantalum under extreme tensile stress," Sci. Adv. **3**, e1602705 (2017).
[22]A. Schropp, R. Hoppe, V. Meier, J. Patommel, F. Seiboth, Y. Ping, D. G. Hicks, M. A. Beckwith, G. W. Collins, A. Higginbotham, J. S. Wark, H. J. Lee, B. Nagler, E. C. Galtier, B. Arnold, U. Zastrau, J. B. Hastings, and C. G. Schroer, "Imaging shock waves in diamond with both high temporal and spatial resolution at an XFEL," Sci. Rep. **5**, 11089 (2015).
[23]B. Nagler, A. Schropp, E. C. Galtier, B. Arnold, S. B. Brown, A. Fry, A. Gleason, E. Granados, A. Hashim, J. B. Hastings, D. Samberg, F. Seiboth, F. Tavella, Z. Xing, H. J. Lee, and C. G. Schroer, "The phase-contrast imaging instrument at the matter in extreme conditions endstation at LCLS," Rev. Sci. Instrum. **87**, 103701 (2016).
[24]D. S. Hodge, A. F. T. Leong, S. Pandolfi, K. Kurzer-Ogul, D. S. Montgomery, H. Aluie, C. Bolme, T. Carver, E. Cunningham, C. B. Curry, M. Dayton, F.-J. Decker, E. Galtier, P. Hart, D. Khaghani, H. Ja Lee, K. Li, Y. Liu, K. Ramos, J. Shang, S. Vetter, B. Nagler, R. L. Sandberg, and A. E. Gleason, "Multi-frame, ultrafast, x-ray microscope for imaging shockwave dynamics," Opt. Express **30**, 38405 (2022).
[25]J. Hagemann, M. Vassholz, H. Hoeppe, M. Osterhoff, J. M. Rosselló, R. Mettin, F. Seiboth, A. Schropp, J. Möller, J. Hallmann, C. Kim, M. Scholz, U. Boesenberg, R. Schaffer, A. Zozulya, W. Lu, R. Shayduk, A. Madsen, C. G. Schroer, and T. Salditt, "Single-pulse phase-contrast imaging at free-electron lasers in the hard X-ray regime," J. Synchrotron Radiat. **28**, 52–63 (2021).
[26]F. Seiboth, L. B. Fletcher, D. McGonegle, S. Anzellini, L. E. Dresselhaus-Cooper, M. Frost, E. Galtier, S. Goede, M. Harmand, H. J. Lee, A. L. Levitan, K. Miyanishi, B. Nagler, I. Nam, N. Ozaki, M. Rödel, A. Schropp, C. Spindloe, P. Sun, J. S. Wark, J. Hastings, S. H. Glenzer, and E. E. McBride, "Simultaneous 8.2 keV phase-contrast imaging and 24.6 keV X-ray diffraction from shock-compressed matter at the LCLS," Appl. Phys. Lett. **112**, 221907 (2018).
[27]A. Y. Faenov, T. A. Pikuz, P. Mabey, B. Albertazzi, T. Michel, G. Rigon, S. A. Pikuz, A. Buzmakov, S. Makarov, N. Ozaki, T. Matsuoka, K. Katagiri, K. Miyanishi, K. Takahashi, K. A. Tanaka, Y. Inubushi, T. Togashi, T. Yabuuchi, M. Yabashi, A. Casner, R. Kodama, and M. Koenig, "Advanced high resolution x-ray diagnostic for HEDP experiments," Sci. Rep. **8**, 16407 (2018).
[28]G. Rigon, B. Albertazzi, T. Pikuz, P. Mabey, V. Bouffetier, N. Ozaki, T. Vinci, F. Barbato, E. Falize, Y. Inubushi, N. Kamimura, K. Katagiri, S. Makarov, M. J. E. Manuel, K. Miyanishi, S. Pikuz, O. Poujade, K. Sueda, T. Togashi, Y. Umeda, M. Yabashi, T. Yabuuchi, G. Gregori, R. Kodama, A. Casner, and M. Koenig, "Micron-scale phenomena observed in a turbulent laser-produced plasma," Nat. Commun. **12**, 2679 (2021).
[29]S. B. Brown, A. E. Gleason, E. Galtier, A. Higginbotham, B. Arnold, A. Fry, E. Granados, A. Hashim, C. G. Schroer, A. Schropp, F. Seiboth, F. Tavella, Z. Xing, W. Mao, H. J. Lee, and B. Nagler, "Direct imaging of ultrafast lattice dynamics," Sci. Adv. **5**, eaau8044 (2019).
[30]S. F. Wang, Y. F. Hsu, J. C. Pu, J. C. Sung, and L. G. Hwa, "Determination of acoustic wave velocities and elastic properties for diamond and other hard materials," Mater. Chem. Phys. **85**, 432–437 (2004).
[31]R. Ramis, R. Schmalz, and J. Meyer-Ter-Vehn, "MULTI—A computer code for one-dimensional multigroup radiation hydrodynamics," Comput. Phys. Commun. **49**, 475–505 (1988).
[32]J. M. Lang, J. M. Winey, and Y. M. Gupta, "Strength and deformation of shocked diamond single crystals: Orientation dependence," Phys. Rev. B **97**, 104106 (2018).
[33]S. A. Dyachkov, A. N. Parshikov, M. S. Egorova, S. Y. Grigoryev, V. V. Zhakhovsky, and S. A. Medin, "Explicit failure model for boron carbide ceramics under shock loading," J. Appl. Phys. **124**, 085902 (2018).
[34]M. S. Egorova, S. A. Dyachkov, A. N. Parshikov, and V. V. Zhakhovsky, "Parallel SPH modeling using dynamic domain decomposition and load balancing displacement of Voronoi subdomains," Comput. Phys. Commun. **234**, 112–125 (2019).
[35]A. N. Parshikov and S. A. Medin, "Smoothed particle hydrodynamics using interparticle contact algorithms," J. Comput. Phys. **180**, 358–382 (2002).
[36]L. Samoylova, A. Buzmakov, O. Chubar, and H. Sinn, "*WavePropaGator*: Interactive framework for X-ray free-electron laser optics design and simulations," J. Appl. Crystallogr. **49**, 1347–1355 (2016).